Acta Crystallographica Section A
Foundations of Crystallography
ISSN 0108-7673

Received 18 July 2005
Accepted 21 August 2005

Double-helix structure in multiwall boron nitride nanotubes

Ayten Celik-Aktas,[a] Jian-Min Zuo,[b]* James F. Stubbins,[a] Chengchun Tang[c] and Yoshio Bando[c]

[a]Department of Nuclear, Plasma, and Radiological Engineering, University of Illinois at Urbana-Champaign, IL 61801, USA, [b]Department of Materials Science and Engineering and Frederick Seitz Materials Research Laboratory, University of Illinois at Urbana-Champaign, IL 61801, USA, and [c]National Institute for Research in Inorganic Materials, Tsukuba, Ibaraki 305-0044, Japan. Correspondence e-mail: jianzuo@uiuc.edu

A new nanotube structural form is reported that resembles a double helix in multiwall boron nitride nanotubes (MW-BNNT) grown by a carbon-free chemical-vapor-deposition process as documented by evidence obtained by transmission electron diffraction and microscopy. The double-helix structure is found in MW-BNNTs exhibiting the same chirality in its different walls. The MW-BNNTs deviate from the structure of ideal nested coaxial cylindrical tubes. Most significantly, bright- and dark-field electron imaging reveals regular zigzag dark and bright spots on the side walls of the nanotubes. The repeating distance between the bright, or dark, spots is related to the chiral angle of the nanotube. Electron diffraction patterns recorded from individual nanotubes show additional diffraction spots belonging to the ⟨201⟩ zone axes, which are not allowed in a perfectly cylindrical nanotube. These additional diffraction spots become asymmetrical as smaller sections of the nanotube are probed. A series of diffraction patterns recorded along the tube axis showed that the imperfections giving rise to these spots move in a regular fashion around the circumference of the tube. It is shown that all experimental evidence supports the structure model of two helices; one is polygonal in cross section and highly crystalline and the other is circular and less ordered. It is further suggested that the double-helix structure is a result of stronger wall–wall interactions associated with the ionic bonding in boron nitride.

1. Introduction

The discovery of carbon nanotubes (CNT) by Iijima (1991) and the consequent development of large-scale synthesis methods has stimulated great interest in other forms of nanotubes, or tubular structures, and their unique electronic, mechanical and chemical properties. As a result of the intensified research, it is now recognized that nanotube formation is not limited to carbon and is a general feature of many layered materials. For example, a number of nanotube structures have been synthesized from BN, WS_2, MoS_2, $NbSe_2$, $NiCl_2$, SiO_2, TiO_2, MoO_3 and V_2O_5 (Pokropivnyi, 2001).

BN nanotubes (BNNT) have received significant interest as an alternative to CNTs since their first successful synthesis by Chopra *et al.* (1995). Hexagonal BN is similar in structure to graphite that forms CNTs. BN nanotubes possess physical, chemical and electronic properties that provide potential advantages over CNTs. For example, individual CNTs can be either metallic or semiconducting depending on the tube diameter and chirality. However, BN nanotubes are expected to have a constant band gap (∼5.5 eV) regardless of the tube chirality and diameter (Blase *et al.*, 1994). In addition, BNNTs have high oxidation resistance (onset temperature for oxidation is ∼1073 K) compared to 673 K for CNTs (Chen *et al.*, 2004). Tubular hexagonal BN also exhibits piezoelectricity (Mele & Kral, 2002; Nakhmanson *et al.*, 2003; Sai & Mele, 2003).

Multiwall BN nanotubes show several structural differences from their carbon counterparts. Most multiwall carbon nanotubes consist of tubes of different chiral angles (mixed chirality) and, in some cases, bunching of chiralities was observed (Bernaerts *et al.*, 1998). In contrast, the chiral angles of different walls in many multiwall BN nanotubes are distributed, or grouped, around a single chiral angle in a narrow angular range (single chirality) (Celik-Aktas *et al.*, 2005). Furthermore, additional graphitic diffraction spots are often observed in multiwall BN nanotubes. Conventional transmission electron microscopy (TEM) imaging of BN nanotubes also shows regular occurrences of regions with dark contrast along the tube axis, which was reported before but has not been explained (Ma *et al.*, 2002; Terrones *et al.*, 2003; Xu *et al.*, 2004; Tang *et al.*, 2004). In contrast to BN nanotubes,

additional graphitic diffraction spots and regions with dark contrast are rarely observed in CNTs (Bernaerts *et al.*, 1998; Zhang *et al.*, 2005).

Here we show that multiwall BN nanotubes of single chirality type consist of regions of highly ordered crystalline BN and less-ordered BN layers. The ordered BN forms a highly regular helical structure. The helical pitch distance is strongly correlated with the tube chirality. Experimental evidence also suggests that the helix is faceted. The overall tube structure, in many cases, resembles a double-helix structure; one almost crystalline and the other made of defective layered BN. The structure was revealed by a detailed investigation of the dark spots and defects of multiwall BN nanotubes. Electron imaging and diffraction patterns from nanometre-sized sections of multiwall BN nanotubes are employed to investigate the structures, especially the origin of regular dark regions in bright-field TEM images of the tubes.

The key experimental evidence comes from electron diffraction. To help with interpretation of nanotube diffraction patterns, §§2 and 3 first review the current structural models of multiwall nanotubes and the diffraction theory of helical structures, respectively. Simulated diffraction patterns of perfectly cylindrical and polygonal nanotubes are presented in §3. The theoretical results will be used for comparison with experimental diffraction patterns. The experimental techniques used for this study are described in §4. §5 contains the results of BN nanotube structure investigation and discussions, which is then followed by conclusions in §6.

2. Structural models of multiwall nanotubes

In order to place the results that will be presented in this paper in a proper context, it is helpful to review our current understanding of nanotube structures.

A single-wall nanotube is considered as formed by rolling up a rectangular sheet of periodical atoms in a two-dimensional lattice into a perfect cylinder. The structure of the tube is described by the chiral vector $\mathbf{C} = n\mathbf{a} + m\mathbf{b}$, where n and m are integers and $\mathbf{a}$ and $\mathbf{b}$ are the two-dimensional lattice vectors. The length of $\mathbf{C}$ gives the tube circumference and the angle between $\mathbf{C}$ and $\mathbf{a}$ is the tube chiral angle.

A double-wall nanotube is made of two coaxial cylindrical tubes. An ideal multiwall nanotube is made of nested coaxial cylindrical tubes (the 'Russian doll' model), where the interlayer bonding is much weaker than the intralayer bonding. The Russian doll structure model is widely accepted for multiwall carbon nanotubes. In a multiwall carbon nanotube, the neighboring layers are incommensurate in general, *i.e.* each layer has its own chirality independent of other layers. On rare occasions, grouping of chiral angles were observed (Ruland *et al.*, 2003; Zhang *et al.*, 2005; Koziol *et al.*, 2005) in carbon nanotubes grown by chemical vapor deposition (CVD). Clustering of chiral angles was explained by a layer-by-layer growth mechanism (Zhang *et al.*, 2005). In the work of Koziol *et al.* (2005), nitrogen was introduced into the growth chamber and the resulting multiwall carbon nanotubes contained about 3% nitrogen. However, the role of nitrogen in the grouping of chiral angles was not clear.

Two alternative models to the ideal nested coaxial cylindrical tube structure have been suggested. One is the scroll model in which the entire multiwall nanotube is a roll-up of a single two-dimensional sheet like a paper roll. In the publication of Ruland *et al.* (2003), grouping of chiral angles in multiwall carbon nanotubes was cited as evidence for the 'scroll' structural model. It is worthwhile noting that the scroll structure in general can be formed from a strained thin solid film (Schmidt & Eberl, 2001). The scroll structure has also been found in oxide nanotubes (Chen *et al.*, 2002).

Another tube model consists of polygonal, rather than cylindrical, tubes. Polygonal cross sections in multiwall CNT have been observed. For example, additional graphitic diffraction spots were observed by Bernaerts *et al.* (1998) on multiwall CNTs. The additional diffraction spots were attributed to deviations from the perfect cylindrical geometry and polygonal nanotube cross sections. In another study on multiwall CNTs, asymmetric layer spacing was observed on two sides of the tube, which was cited as direct evidence of polygonal tube cross section (Liu & Cowley, 1994). It is important to note here that the large layer spacing was uniform along the tube axis, which suggests a uniform polygonal section along the nanotube axis.

3. Diffraction from nanotubes

Here we outline the diffraction theory of nanotubes, which forms the foundation for interpretation of electron diffraction patterns. Electron diffraction theory of carbon nanotubes has been developed by Lambin & Lucas (Lambin & Lucas, 1997; Lucas & Lambin, 2005) and Qin (2001). The theory is based on diffraction from helical structures and the kinematic approximation. Compared to electron diffraction from crystals, the dynamic effect is negligible for carbon and BN nanotubes because of the weak atomic scattering and the small structure. The details of diffraction theory from helical structures, which was originally developed for the α-helix conformation of proteins, can be found in standard textbooks, see Sherwood (1976).

In the kinematic approximation, a diffraction pattern is described by the amplitude squared of the Fourier transform of the potential. The Fourier transform of a single strand of atoms periodically arranged along a helix involves four components: (i) the transform of atomic potentials, which gives atomic scattering factors; (ii) the transform of the helix; (iii) the transform of the pitch function (spacing P); and (iv) the transform of the plane function (spacing p). Both pitch and plane functions are one-dimensional periodic δ functions with periods P and p, respectively. The Fourier transform of the pitch function is an infinite array of reciprocal planes with spacing $1/P$. The Fourier transform of the plane function is an infinite array of reciprocal planes with spacing $1/p$ (note that $P > p$ for most chiral tubes). The Fourier transform of a single turn of a helix is more complicated (see Sherwood, 1976, for details of derivation). The result given below is for a circular

helix in the cylindrical reciprocal coordinates (R, ψ, ξ), which relates to the Cartesian coordinates by $k_x = R\cos\psi$, $k_y = R\sin\psi$ and $k_z = \xi$:

$$F_k(R, \psi, \xi) = F_k(R, \psi, N/P) = r_k \exp[iN(\psi + \pi/2 - \theta_k)] J_N(2\pi R r_k) \quad (1)$$

with $J_N(X)$ as the Bessel function of order N, which comes from the Fourier transform of the circular tube cross section. Nanotube diffraction occurs at $\delta(k_z - N/P - M/p)$ with both N and M integers. Thus, for nanotube diffraction, it must satisfy the following selection rule:

$$k_z = N/P + M/p, \quad (2)$$

where

$$P = |\mathbf{C}| \tan\alpha = a(n^2 + m^2 - nm)^{1/2} \frac{3^{1/2} m}{2n - m} \quad (3)$$

and

$$p = a\sin\alpha = a\frac{3^{1/2}}{2(n^2 + m^2 - nm)^{1/2}}. \quad (4)$$

Here (n, m) are the chiral indices and α is the chiral angle of the nanotube. For carbon nanotubes, the graphene sheet has a non-primitive unit cell with two independent atoms, each constituting a primitive helix. For a chiral tube, there are also multiple unit cells in the repeat distance P. The total structure factor then is a sum of contributions from multiple helices and the structure factor of a single-wall nanotube in general is given by

$$F_k(R, \psi, \xi) = \sum_N r_k \exp[iN(\psi + \pi/2)] J_N(2\pi R r_k) \times \sum_j f_j \exp\left[i\left\{-N\theta_{jk} + 2\pi\left(\frac{N}{P} + \frac{M}{p}\right) z_{jk}\right\}\right], \quad (5)$$

where the relative phase of each helix is accounted for in the complex exponential. The structure factor of a multiwall concentric nanotube is the sum of the structure factors of single-wall nanotubes:

$$F(R, \psi, \xi) = \sum_k F_k(R, \psi, \xi). \quad (6)$$

Overall, the diffraction pattern from a circular nanotube lying horizontally and the electron beam along the vertical direction consists of two components. (i) Diffraction from the atomic structure of the hexagonal sheet in the form of layer lines with modulations as described by high-order Bessel functions [see equation (5)]. The oscillations in the layer lines are elongated normal to the tube axis because electron waves see a shrinking lattice parameter along the tube circumference owing to curvature of the nanotubes. The modulations are caused by the interference of diffracted waves from right and left sides of the nanotube. (ii) Equatorial oscillations from the cylindrical tube geometry which result in $(0, 0, 2n)$ types of diffraction spots.

Fig. 1(*a*) shows the diffraction pattern of a (54, −40) single-wall BN nanotube simulated by kinematic theory. We can clearly see the layer lines predicted by helical diffraction theory. Each layer line has its own oscillations, which are determined by the order of the Bessel function as expected from the above formulations and discussions. Each layer line is mirror symmetric with two Bessel functions in opposite directions (the structure factor only depends on the radius). Each can be indexed based on the two-dimensional hexagonal lattice. The relationship between the hexagonal index and the order of Bessel function is given in equation (5). Overall, the diffraction pattern has $2mm$ symmetry.

Fig. 1(*b*) shows the simulated diffraction pattern of a 10-wall BN nanotube. For high-order layer lines, there is no interference between different walls in the case of an incommensurate nanotube. Interference only occurs when two or more walls have the same chiral angle. Thus, for incommensurate tubes, the intensity of high-order layer lines is simply the summation of diffraction intensity from individual single-wall nanotubes.

Diffraction from a polygonal tube is more complicated owing to the loss of cylindrical symmetry. The electron diffraction pattern depends on the relative orientation between the incident beam and the tube. To see this effect, we have simulated electron diffraction of a polygonal nanotube in two different orientations with respect to incident beam. The results are shown in Figs. 1(*c*) and (*d*). Nanotubes were formed by folding the BN sheet of the same chirality as Fig. 1(*a*) into a hexagonal tube. Depending on the relative orientation of the hexagonal nanotube with respect to the electron beam,

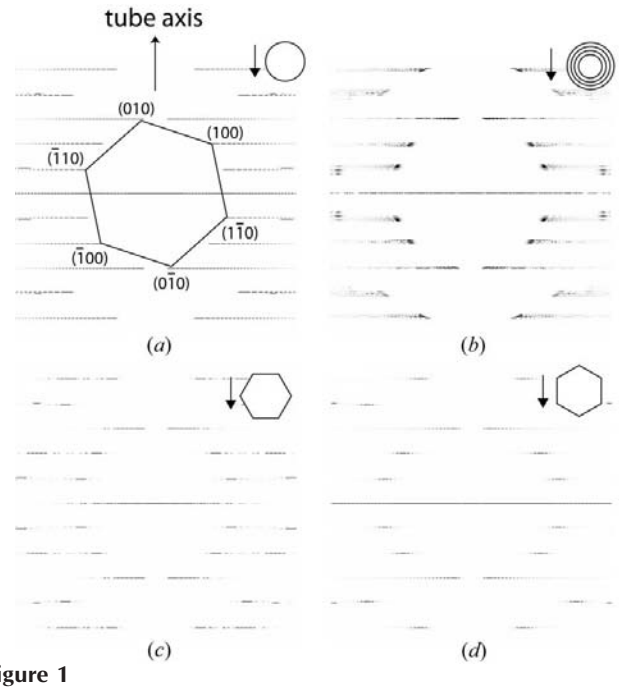

Figure 1
Diffraction patterns of circular and hexagonal nanotubes simulated by kinematic diffraction theory. (*a*) Diffraction pattern of a (54, −40) single-wall BN nanotube. (*b*) Simulated diffraction pattern of a 10 wall BN nanotube. The inner diameter is 4.7 nm and the outer diameter is 10.8 nm. (*c*) Diffraction pattern of a (54, −40) tube shaped into a hexagonal prism. (*d*) Same as (*c*) but the tube is rotated 30° clockwise. Insets in (*c*) and (*d*) show the orientation of the hexagonal tubes with respect to the electron beam.

different graphitic diffraction spots are excited (see Figs. 1*c* and *d*).

4. Experimental procedures

The boron nitride nanotubes studied here were grown in a carbon-free chemical-vapor-deposition process at 1373 K (Tang *et al.*, 2002). The tube outer diameters range from 12 to 80 nm and the inner diameters range from 3 to 18 nm. Tubes were straight and long, lengths reaching up to 10 μm. Sample preparation was accomplished by depositing BNNTs from a dispersion of nanotubes in acetone onto copper grids covered with a holey carbon film and allowing the solvent to evaporate. TEM studies were carried out with a JEOL 2010F TEM at a high voltage of 200 keV. Dark-field and bright-field imaging, nanoarea electron diffraction (NED), electron-energy-loss spectroscopy (EELS), and energy-dispersive X-ray (EDX) analysis were used to characterize the nanotubes.

To record electron diffraction patterns from individual nanotubes with high angular resolution, we have used the NED technique. In the NED mode, the electron beam is focused at the front focal plane of the objective lens using the third condenser lens in the JEOL 2010F electron microscope. As a result, the sample is illuminated with a small probe of a nearly parallel electron beam. Since no selected-area aperture is used in this process, no electrons scattered by the sample are thrown away. Therefore, diffraction intensity is higher than it would be in the selected-area diffraction mode. The size of the

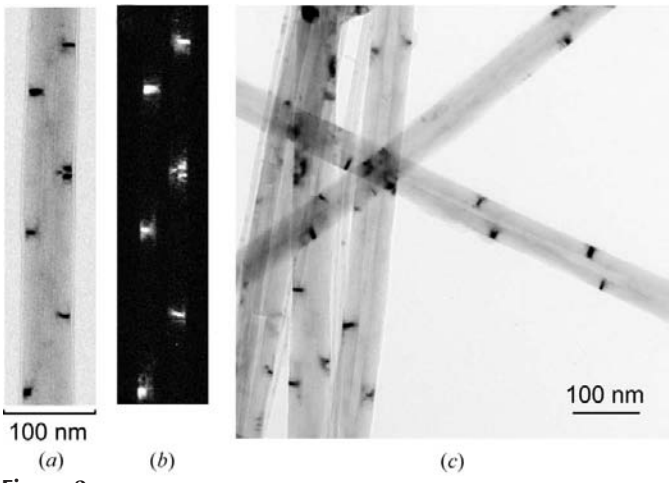

Figure 2
(*a*) Conventional bright-field image of a multiwall BN nanotube. (*b*) Central dark-field image of the same area as (*a*). (*c*) Conventional TEM image of the CVD-grown multiwall BN nanotubes showing regular dark spots.

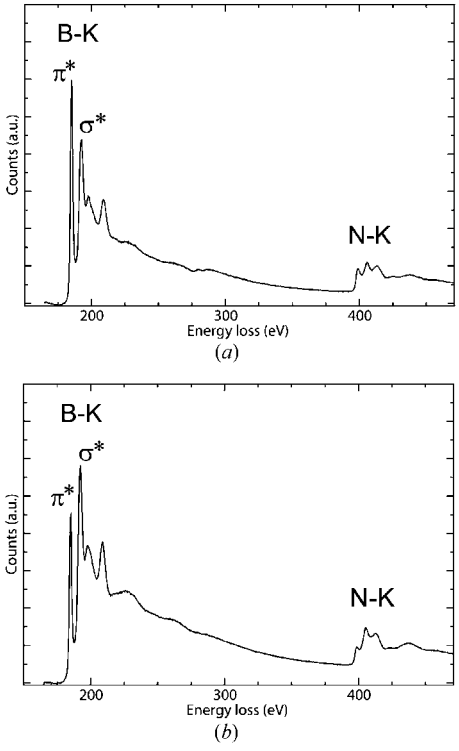

Figure 3
EELS spectra obtained from (*a*) BN nanotube side walls with dark contrast and (*b*) without dark contrast. The background is subtracted in both cases.

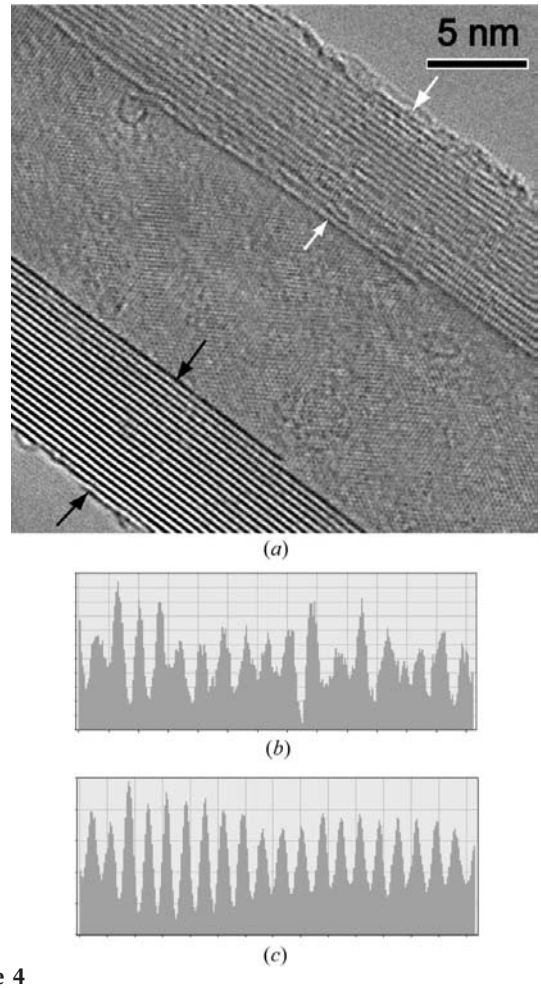

Figure 4
(*a*) HRTEM image showing the difference between the side walls of a multiwall BN nanotube. There was a dark spot on the side marked with black arrows. Upon high-resolution imaging, the dark region of the nanotube appears more crystalline than the opposite side wall. (*b*) Line scan from the side wall marked with white arrows. (*c*) Line scan from the side wall with a dark region marked with black arrows.

condenser aperture controls the final beam size and the intensity of the beam. For the results presented in this report, the smallest probe used was 50 nm in diameter, which was obtained by using a condenser aperture of 10 μm in diameter. High-resolution electron diffraction patterns of BN nanotubes were digitally recorded on Fuji imaging plates with a camera length of 80–100 cm.

5. Results and discussion

Figs. 2(*a*) and (*b*) show the conventional bright- and dark-field images of a representative multiwall BN nanotube. A striking feature of the tube is the regular dark (or bright) spots observed on both sides of the nanotubes in bright- (or dark-) field imaging mode. Furthermore, these spots repeat almost regularly in a zigzag pattern in projection as observed in electron microscopy. The appearance of regular spots was common in many BN nanotubes that we have characterized (see Fig. 2*c*). To investigate the origin of the observed dark spots, we looked for evidence of change in both chemical composition and structure along the tube axis.

EELS and EDX analyses were carried out to probe compositional change between the dark regions and the rest of the tubes. EELS measurements were recorded from different locations along the tube axis at a fixed radial distance. Both EELS and EDX results did not show the presence of any significant impurity. This is in contradiction to the recent report by Kim *et al.* (2005), in which they attributed the dark spots along the multiwall BN nanotubes and the contrast difference to compositional change. It must be noted that our EELS study did reveal a significant difference in the ratio of π^* and σ^* peaks measured at the dark spots and at the other locations. The difference is due to the change in the relative orientation of the *c* planes with respect to the electron beam across the tube axis (see Figs. 3*a* and *b*).

To investigate possible structure variations along the tube, the dark-field imaging technique was used. Dark-field images were formed by using the 002 spot along the equatorial line of the nanotube diffraction pattern. The dark regions in the bright-field image appeared bright in the dark-field image, indicating that these regions contribute to a strong 002 peak (see Fig. 2). From this, we conclude that the regions in the bright field appear darker than the rest of the tube owing to diffraction contrast. The 002 peak is formed by interference between the different walls of the nanotube. For a circular multiwall tube, the intensity of the 002 peak depends on the regularity of the wall spacing and the number of walls. If the multiwall tube is faceted, the peak intensity also depends on the relative orientation between the electron beam and the facet. In other words, those regions that satisfy the Bragg diffraction condition and have regular wall spacing are where more electrons are scattered, so fewer electrons in the dark regions are contributing to the bright-field TEM image.

High-resolution transmission-electron-microscopy (HRTEM) imaging of the dark regions on the side walls revealed high crystallinity compared to other side walls of the nanotube (see Fig. 4*a*). The image contrast is also much higher in the dark region. The HRTEM images were recorded under the condition close to the Scherzer defocus with an information transfer up to 0.14 nm. Measurements on HRTEM images show that the spacing in the dark regions is regular with an average layer separation of 0.347 ± 0.006 nm, Fig. 4(*c*). However, spacing on the opposite side of the tube is irregular with an average spacing of 0.366 ± 0.035 nm, Fig. 4(*b*). For reference, the interlayer spacing of bulk hexagonal BN (hBN) is 0.335 nm. Thus, the interlayer spacing of BN nanotubes is larger than bulk hBN and varies from place to place along BN nanotubes. In comparison, interlayer spacing of carbon nanotubes was found to be 0.344 nm, which is also larger than that in bulk graphite (Saito & Yoshikawa, 1993).

To further investigate the placement of 'dark spots' in the multiwall BN nanotubes and its dependence on diffraction conditions, a tilting experiment was carried out. We carefully selected an intersection of three tubes (two of the three are almost perpendicular to each other). The intersection point

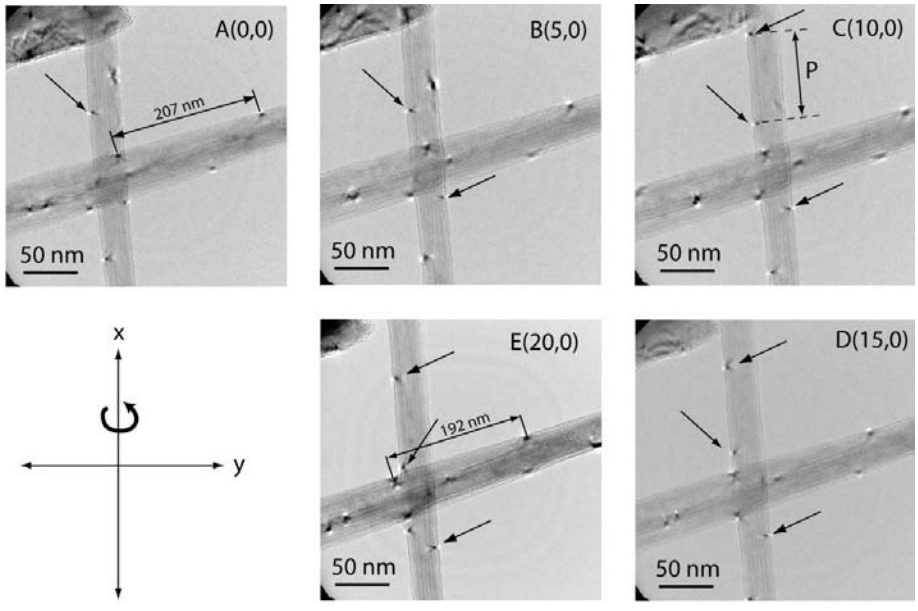

Figure 5
Results of tilting experiments showing the movement of the dark spots along the side walls of the BN nanotubes. Pitch distance (*P*) between two consecutive dark spots has remained constant along the vertical tube, which was almost parallel to the rotation direction, whereas the distance between the dark spots on the horizontal tube has become shorter owing to rotation (see *A* and *E*). The numbers in parentheses represent the amount of rotation in degrees.

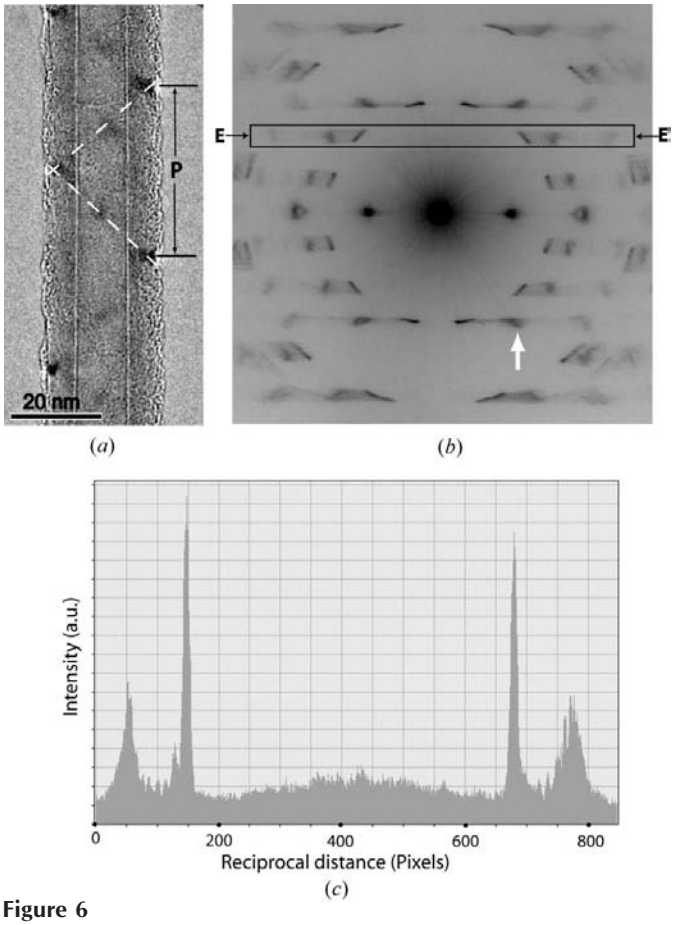

Figure 6
(*a*) TEM image of a representative BN nanotube. Dark contrast regions in the middle of the tube as well as on the side walls are visible. (*b*) Electron diffraction pattern of the nanotube shown in (*a*). Chiral angles of the different layers have grouped around an average chiral angle of 12.8°. (*c*) Intensity profile from the rectangular region along (*EE*′) of (*b*).

was used as the imaging reference. Then, using a double-tilt sample holder, the specimen was rotated in 5° increments from 0 to 20° around the *x* axis (*x* and *y* axes are defined in Fig. 5), which is almost parallel to the vertical tube (see Fig. 5). The resulting new images were recorded in the TEM mode. As the sample was rotated around the *x* axis, the dark spots in the vertical tube, which are marked with arrows, moved downward along the *x* axis (see Figs. 5*A*–*E*), while the relative distance between the consecutive dark spots (pitch distance) remained approximately constant (see Figs. 5*C*–*E*). Spacing between dark spots on the horizontal tube became shorter as marked on Figs. 5(*A*) and (*E*). The shorter distances are easily explained by the change in projection owing to rotation. For the vertical tube, the fact that the dark spots move downwards while the distance between them remains constant suggests that the dark regions are continuous and helical around the nanotube. Thus, instead of dark spots, these features might be better called 'helical dark ribbons'.

Figs. 6(*a*) and 7(*e*) show multiwall BN nanotubes with periodic dark spots on the side walls as well as in the middle section of the tube. The dark-contrast regions in the middle part lie on the straight lines connecting the consecutive dark spots on the opposite sides of the nanotube (see dashed white lines on Fig. 6*a*). The dark contrast is related to strong diffraction condition (see discussion below about diffraction symmetry). Placement of dark spots with respect to each other in projection is mostly triangular as in Figs. 6(*a*) and 7(*e*), further supporting a three-dimensional structure with the dark regions helically wrapping around the tube. In some cases, rectangular arrangements of dark spots were observed as well. We speculate that in some of those cases there might be more than one (probably two) highly crystalline 'helical ribbons' that are winding around the nanotube.

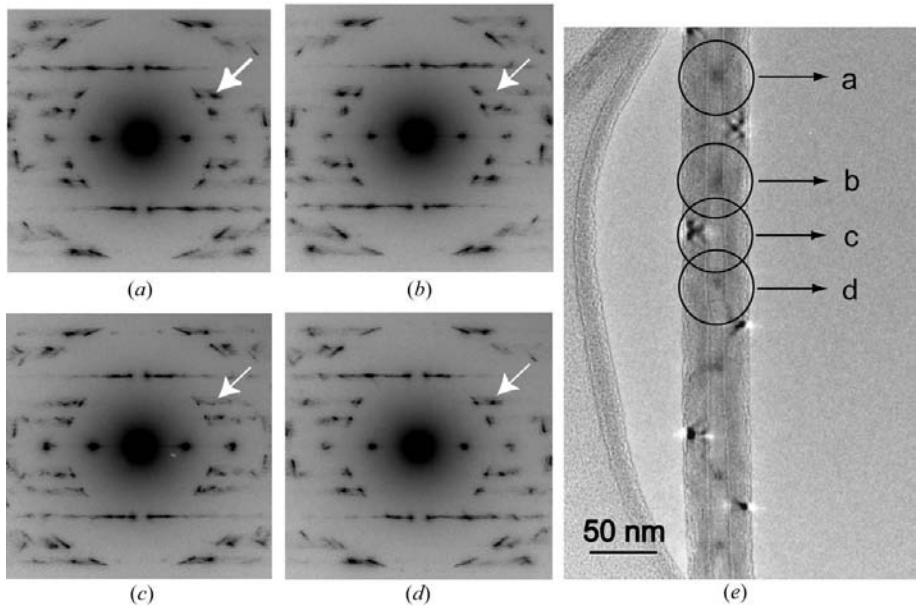

Figure 7
(*a*)–(*d*) Series of electron diffraction patterns recorded from the areas marked in (*e*). (*e*) TEM image of a multiwall BN nanotube showing the locations of the areas used in the diffraction study.

A major difference between multiwall carbon and BN nanotubes is the chirality distribution of different walls. In general, the chirality of each layer in a multiwall carbon nanotube is independent of the others, whereas BN tubes show grouping of chiral angles around an average value (Celik-Aktas *et al.*, 2005). An example of multiwall BN nanotube electron diffraction patterns is shown in Fig. 6(*b*). It was recorded in the NED mode with an electron probe of 125 nm diameter. The chiral angles of different layers in this multiwall nanotube grouped around an average chiral angle of 12.8° with a distribution of ±2.1°. Compared to the simulated multiwall nanotube diffraction pattern of Fig. 1(*b*),

there are additional graphitic diffraction spots in the experimental pattern, *e.g.* the spot pointed out by the white arrow in Fig. 6(*b*).

The spacing of dark spots on BN nanotube side walls that were observed in bright-field TEM images is directly correlated to the average chiral angle of the BN nanotube. Fig. 8 shows the average chiral angle *versus* the ratio of the pitch distance (*P*) and outer diameter (OD) in multiwall BN nanotubes. There is a close correlation between the chiral angle of the nanotube and the *P*/OD ratio up to 15°. Even though approximately equal numbers of BN nanotubes both above and below the 15° boundary are observed, nanotubes with chiral angles >15° tend to have an irregular arrangement of dark spots along the tube axis. For this reason, the curve fitting was not extended beyond chiral angles larger than 15°.

Using the NED technique and a small electron probe of 50 nm in diameter, we probed the local structure along the BN nanotube. Figs. 7(*a*)–(*d*) show the electron diffraction patterns obtained from four different places of Fig. 7(*e*) along a 38 nm diameter BN nanotube. These diffraction patterns were recorded with a condenser aperture of 10 µm in diameter, which produces a parallel electron beam of about 50 nm in the NED mode. As a result, it was possible to resolve structure variations of length scale of tens of nanometres along the tube. All four diffraction patterns from small sections of the nanotube lack the 2*mm* symmetry that characterizes the simulated electron diffraction patterns of perfectly circular tubes [see Figs. 1(*a*) and (*b*) and discussion of 2*mm* symmetry in §3]. Diffraction pattern (*a*) is a mirror image of (*b*), while (*d*) is similar to (*a*). There is no clear distinction between the top and the bottom surfaces of the nanotube when the dark spot is seen on the side walls of the tube (see Fig. 7*c*). However, in (*a*), (*b*) and (*d*), dark-contrast regions are in the middle part of the tube. It is evident from Figs. 7(*a*), (*b*) and (*d*) that the structure giving rise to the {112} spot (marked by white arrows) flip-flops between the two hexagons that belong to the top and bottom surfaces of the tube. In comparison to Fig. 6(*b*), which was recorded with a 125 nm probe, there were six dark spots on the side walls and five dark regions in the middle section of the nanotube contributing to the diffraction. In this case, a complete set of {112}-type secondary spots was observed. As a result, the diffraction pattern mimics the 2*mm* symmetry. However, the intensity profile in the boxed region along the *EE*′ direction of Fig. 6(*b*) shows small differences between mirror-related diffraction spots, indicating imperfections in the helical structure (see Fig. 6*c*).

The asymmetry in the recorded electron diffraction patterns shown in Fig. 7 is directly correlated with contrast variations observed in electron images. Figs. 9(*b*) and (*c*) show the fast Fourier transform (FFT) patterns obtained from two square regions as indicated in Fig. 9(*a*) where the HRTEM image shows significantly darker contrast. The FFT patterns show additional frequencies that are consistent with the additional spots in the diffraction patterns of Fig. 7. In the FFT of the region bounded by square (1), the spot on the left-hand side of the equatorial line marked with *X* has higher intensity than the corresponding spot on the right-hand side (marked with *Y*) (see Fig. 9*b*). The FFT of region (2) is shown in Fig. 9(*c*). In this case, spot *Y* has higher intensity than spot *X*. Thus, Fig. 9(*c*) is almost a mirror image of Fig. 9(*b*). The asymmetric behavior of the BN nanotubes that we see in electron diffraction patterns is also reproduced in electron images. The resolution of the FFT-produced diffraction patterns is much lower than the resolution of directly recorded electron diffraction patterns. However, the side length of each square region used in the FFT is only 10 nm, which is much smaller than the electron probe size used in diffraction.

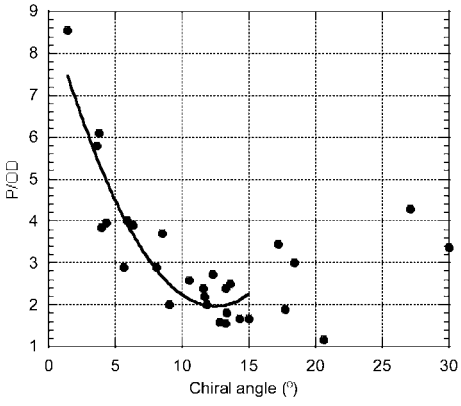

Figure 8
Average chiral angle *versus* the ratio of pitch distance between dark spots (*P*) and outer diameter (OD) in multiwall BN nanotubes. The continuous curve is a second-order polynomial fit to the experimental data.

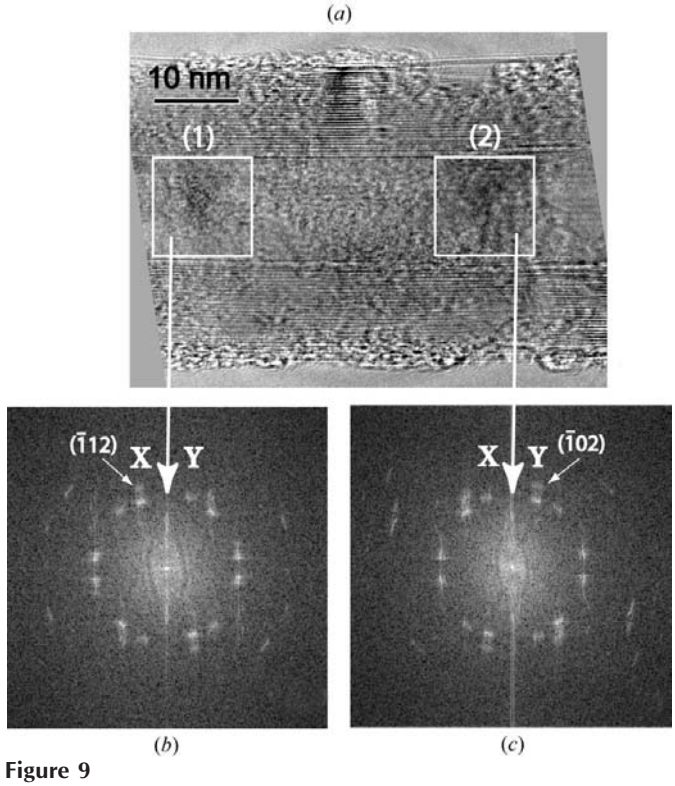

Figure 9
(*a*) HRTEM image of a multiwall BN nanotube. (*b*) FFT of the region bounded by square (1) of the TEM image. (*c*) FFT of the region bounded by square (2) on the right-hand side of the TEM image.

The symmetry-breaking diffraction spots observed in both diffraction patterns and FFTs of HRTEM images indicate that the nanotube, or at least part of it, is faceted. Fig. 10 indexes the diffraction pattern shown in Fig. 7(*a*). The two hexagons in Fig. 10 indicate diffraction spots from the hexagonal BN for upper and lower halves of the tube. The equatorial line is marked by two horizontal arrows. For multiwall nanotubes, the interference between different walls produces sharp diffraction spots along the equatorial line; the first diffraction spot can be indexed as the 002 of hexagonal bulk BN. Both the hexagons and equatorial line are expected from ideal cylindrical tubes as we have shown in §3. What are not expected are those additional diffraction spots, especially the symmetry-breaking ones, which are marked by circles and vertical arrows. The diffraction spots marked by circles belong to either the [201] or the [$\bar{2}$01] zone axes. Other prominent diffraction spots are (01$\bar{2}$), (01$\bar{3}$) and (01$\bar{4}$) reflections, which are marked by arrows. The presence of these additional diffraction spots suggests that at least part of the tube is faceted [additional graphitic diffraction spots have been observed previously on multiwall CNT diffraction patterns and they were attributed to polygonal nanotube cross sections (Bernaerts *et al.*, 1998)]. The [201] and [$\bar{2}$01] zones are at $\pm35.7^\circ$ to the [001] or $\pm54.3^\circ$ to the [100]. The (01$\bar{2}$), (01$\bar{3}$) and (01$\bar{4}$) reflections belong to zone axes [*u*21], [*u*31] and [*u*41]. The precise value of *u* is not known, but a low integer value for *u* can be ruled out because of the lack of zone-axis diffraction patterns associated with those reflections. All of the additional diffraction spots are associated with one of the two hexagons and thus from faceting in either the upper or the lower half of the tube, but not both. Correspondingly, the diffraction pattern shown in Fig. 7(*b*) can be attributed to faceting in the half with zone axes in opposite directions.

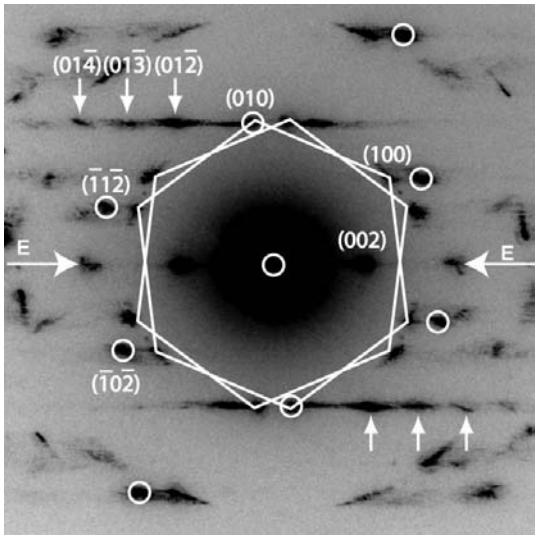

Figure 10
The same diffraction pattern as in Fig. 7(*a*). Diffraction spots marked by two hexagons are due to the honeycomb lattice of top and bottom surfaces of the nanotube. Additional graphitic spots are marked with white circles and arrows. The circles belong to the [$\bar{2}$01] zone axis of hexagonal BN.

The faceting observed here is very different from that observed in some multiwall carbon nanotubes by Liu & Cowley (1994) and in BN nanotubes formed by arc discharge (Saito *et al.*, 1999). In both of these cases, faceting is observed uniformly along the tube, which is very different from the zigzag pattern observed here. In the study of Liu & Cowley (1994), a multiwall CNT with larger layer spacing on one side of the tube has been observed, which was attributed to polygonal tube cross section. It is important to note here that the larger layer spacing was uniform along the tube axis, which suggests a perfectly polygonal prism aligned with the nanotube axis. Our results on multiwall BN nanotubes suggest a polygonal cross section where the flat portions of the tube which result in additional graphitic diffraction spots do not extend unidirectionally with the tube axis.

The experimental evidence of TEM imaging, tilting, diffraction and FFT analysis presented here points to a double-helix structure; helix I contributes to the zigzag dark contrast that we see in projection HRTEM images and additional symmetry breaking diffraction spots observed in nanoarea electron diffraction patterns, while helix II is associated with less regular wall spacings and diffraction spots of circular tubes. Electron diffraction and imaging evidence also shows that helix I is faceted with six major facets: $\pm$[001], $\pm$[201] and $\pm$[$\bar{2}$01]. Based on these observations, we suggest that helix I is made up of polygonized highly crystalline hexagonal BN. A schematic of the proposed structure model for multiwall BN nanotubes is shown in Fig. 11(*a*). Fig. 11(*b*) shows an atomic structure model of a hexagonal helix in the case of a zigzag tube (0 chiral angle). The facet angle is 60° in this case, which is close to the 54.3° between the [001] and [201] or [$\bar{2}$01] facets. Key to the facets is line defects as indicated in Fig. 11(*c*) where the B and N are chemically different from B—N in the two-dimensional graphene sheet. The line defect is along the [120] or [010] direction. Such line defects have also been observed in multiwall carbon nanotubes and

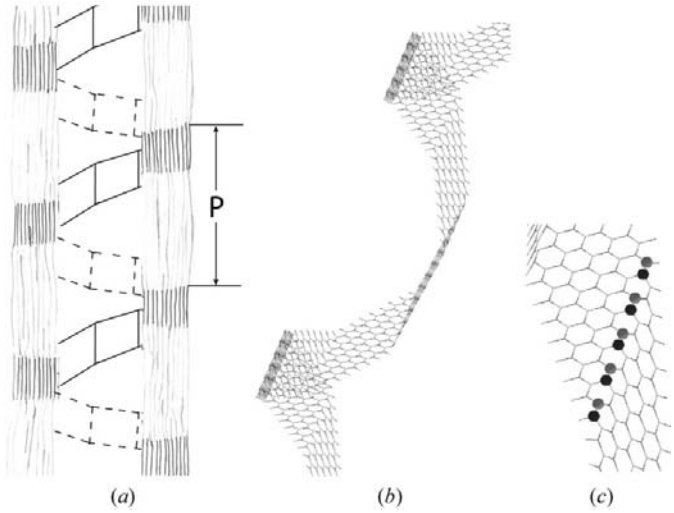

Figure 11
(*a*) Schematic of the proposed structure model for the multiwall BN nanotubes. (*b*) Atomic structure model of a hexagonal helix in the case of a zigzag tube. (*c*) Line defects of an sp^3 bond in BN joining two facets.

have been attributed to sp^3 bonding (Hiura *et al.*, 1994). The same sp^3 bonding is responsible for faceting in BN tubes. In the case of a zigzag tube, the tube axis is parallel to one of the B—N bonds where a single line of defects of sp^3-bonded BN is sufficient to induce folding of the graphene sheet. For a chiral tube, the tube axis is at an angle to the B—N bond and additional defects are needed to fold the graphene sheet along the tube axis. Evidence of these additional defects comes from the presence of high-order facets as evidenced by the presence of $(01\bar{2})$, $(01\bar{3})$ and $(01\bar{4})$ reflections.

As to why multiwall BN forms such a double-helix structure, we speculate that the competition between strain and layer–layer interaction in BN must play an important role. The chirality of BN multiwall nanotubes with double-helix structure is highly correlated, which suggests cohesion between different BN layers to maintain the bulk crystal structure. Other influencing factors include growth kinetics, for example, single strands of polygonal helical ribbons were observed in ZnO (Wang, 2004). What is remarkable about the double-helix structure and other structures, such as helical ribbons and rings, is the complexity of structure in these nanoscale materials.

6. Conclusions

We have presented experimental evidence supporting a new structural model for multiwall boron nitride nanotubes grown by a carbon-free chemical-vapor-deposition process. The evidence, including bright- and dark-field electron imaging reveals regular, zigzag, dark and bright spots on the side walls of the nanotubes, and electron diffraction patterns recorded from individual nanotubes show additional diffraction spots belonging to $\langle 201 \rangle$ zone axes, which are not allowed in a perfectly cylindrical nanotube. The electron diffraction patterns were recorded using nanoarea electron diffraction with a probe size of 125 and 50 nm diameter. A series of diffraction patterns recorded along the tube axis showed that the imperfections giving rise to these spots move in a regular fashion around the tube. Based on this evidence, we suggest a double-helix structural model; one is polygonal in cross section and highly crystalline and the other is circular and less ordered. The double-helix structure is a result of stronger wall–wall interactions associated with the ionic bonding in boron nitride.

Work on electron microscopy characterization was supported by DOE DEFG02-01ER45923 and DEFG02-91ER4539 and uses the TEM facility of the Center for Microanalysis of Materials at Frederick Seitz Materials Research Laboratory at the University of Illinois.

References

Bernaerts, D., Amelinckx, S., Lambin, Ph. & Lucas, A. A. (1998). *Appl. Phys. A*, **67**, 53–64.
Blase, X., Rubio, A., Louie, S. G. & Cohen, M. L. (1994). *Europhys. Lett*. **28**, 335–340.
Celik-Aktas, A., Zuo, J. M., Stubbins, J. F., Tang, C. & Bando, Y. (2005). *Appl. Phys. Lett*. **86**, 133110.
Chen, Q., Zhou, W. Z., Du, G. H. & Peng, L. M. (2002). *Adv. Mater.* **14**, 1208–1211.
Chen, Y., Zou, J., Campbell, S. J. & Caer, G. L. (2004). *Appl. Phys Lett*. **84**, 2430–2432.
Chopra, N. G., Luyken, R. J., Cherrey, K., Crespi, V. H., Cohen, M. L., Louie, S. G. & Zettl, A. (1995). *Science*, **269**, 966–967.
Hiura, H., Ebbesen, T. W., Fujita, J., Tanigaki, K. & Takada T. (1994). *Nature (London)*, **367**, 148–151.
Iijima, S. (1991). *Nature (London)*, **354**, 56–58.
Kim, Y. I., Jung, J. K., Ryu, K.-S., Nahm, S.-H. & Gregory, D. H. (2005). *J. Phys. D: Appl. Phys.* **38**, 1127–1131.
Koziol, K., Shaffer, M. & Windle, A. (2005). *Adv. Mater.* **17**, 760–763.
Lambin, P. & Lucas, A. A. (1997). *Phys. Rev. B*, **56**, 3571–3574.
Liu, M. & Cowley, J. M. (1994). *Carbon*, **32**, 393–403.
Lucas, A. A. & Lambin, P. (2005). *Rep. Prog. Phys.* **68**, 1181–1249.
Ma, R., Bando, Y. & Sato, T. (2002). *Adv. Mater.* **14**, 366–368.
Mele, E. J. & Kral, P. (2002). *Phys. Rev. Lett*. **88**, 56803.
Nakhmanson, S. M., Calzolari, A., Meunier, V., Bernholc, J. & Nardelli, M. B. (2003). *Phys. Rev. B*, **67**, 235406.
Pokropivnyi, V. V. (2001). *Powder Metal. Met. Ceram.* **40**, 582–594.
Qin, L.-C. (2001). *Progress in Transmission Electron Microscopy 2*, edited by X. F. Zhang & Z. Zhang. Berlin: Springer-Verlag.
Ruland, W., Schaper, A. K., Hou, H. & Greiner, A. (2003). *Carbon*, **41**, 423–427.
Sai, N. & Mele, E. J. (2003). *Phys. Rev. B*, **68**, 241405.
Saito, Y., Maida, M. & Matsumodo, T. (1999). *Jpn J. Appl. Phys.* **38**, 159–163.
Saito, Y. & Yoshikawa, T. (1993). *Phys. Rev. B*, **48**, 1907–1910.
Schmidt, O. G. & Eberl, K. (2001). *Nanotechnology*, **410**, 168.
Sherwood, D. (1976). *Crystals, X-rays and Proteins*. New York: John Wiley.
Tang, C., Bando, Y. & Golberg, D. (2004). *J. Solid State Chem*. **177**, 2670–2674.
Tang, C., Bando, Y., Sato, T. & Kurashima, K. (2002). *Chem. Commun.* **12**, 1290–1291.
Terrones, M., Golberg, D., Grobert, N., Seeger, T., Reyes-Reyes, M., Mayne, M., Kamalakaran, R., Dorozhkin, P., Dong, Z.-C., Terrones, H., Ruhle, M. & Bando, Y. (2003). *Adv. Mater.* **15**, 1899–1903.
Wang, Z. L. (2004). *J. Phys. Condens. Matter*, **16**, R829–R858.
Xu, F.-F., Bando, Y., Golberg, D., Hasegawa, M. & Mitome, M. (2004). *Acta Mater.* **52**, 601–606.
Zhang, G. Y., Bai, X. D. & Wang, E. G. (2005). *Phys. Rev. B*, **71**, 113411.